JOURNAL OF FUEL CHEMISTRY AND TECHNOLOGY
Volume 54, Issue 1, January 2026

燃料化学学报(中英文)
Journal of Fuel Chemistry and Technology

Cite this article as: J Fuel Chem Technol, 2026, 54, 20250120

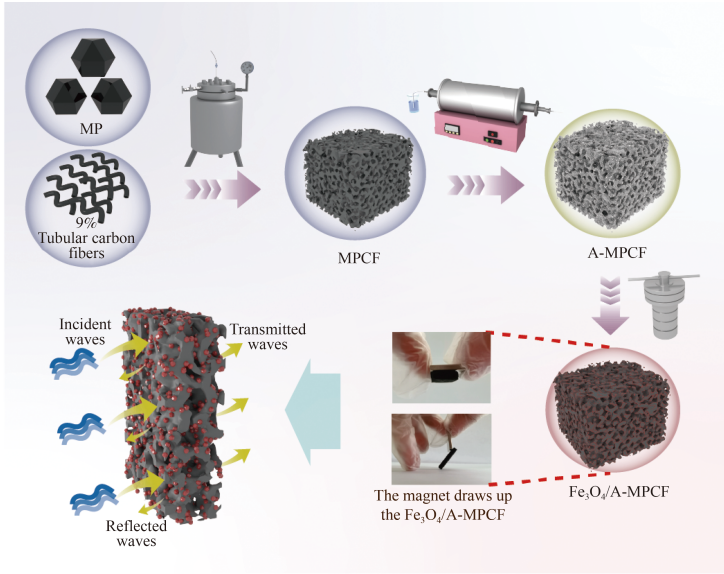
RESEARCH PAPER

Preparation and tailoring electromagnetic shielding and microwave absorbing performance of Fe_3O_4 modified activated carbon foam based on mesophase coal pitch pyrolysis foaming

GE Yuanyuan[1], WANG Yuzhe[1], XU Guozhong[1,*], ZHU Yaming[1], YUAN Xia[2,*], SHI Guimei[3], ZHONG Xiangyun[1]

[1] Engineering Research Center of Coal Chemistry for Liaoning Province, Professional Technology Innovation Center of Coal Chemical Industry for Liaoning, School of Chemical Engineering, University of Science and Technology Liaoning, Anshan 114051, China;
[2] School of Materials Science and Technology, Shenyang Ligong University, Shenyang 110159, China;
[3] School of Science, Shenyang University of Technology, Shenyang 111003, China

Abstract: The development of materials with excellent microwave absorption (MWA) and electromagnetic interference (EMI) shielding performances has currently received attention. Herein, mesophase pitch-based carbon foam (MPCF) with 3D interconnected pore structure was prepared through the high pressure pyrolysis of mesophase coal tar pitch. It is found that the 3D interconnected cellular pores of MPCF facilitate multiple reflections of electromagnetic waves, which results in the minimum reflection loss (RL_{min}) value of MPCF reaches −37.84 dB with the effective absorption bandwidth (EAB) of 5.44 GHz at a thickness of 2.70 mm, and the total average electromagnetic shielding effectiveness (SE_T) under 3.00 mm thickness achieves 26.52 dB in X-band. Subsequently, MPCF is activated by KOH to obtain activated carbon foam (A-MPCF). The average SE_T of A-MPCF achieves 103.00 dB for abundant nanopores on the pore cell walls, which leads to a transition from the multiple reflections of electromagnetic waves on the walls to diffuse reflection. Unfortunately, the reflection coefficient (R) of A-MPCF increases from 0.78 to 0.90. To reduce the R value, Fe_3O_4/A-MPCF was fabricated via the *in situ* growth of nano Fe_3O_4 on A-MPCF. Consequently, the R value of Fe_3O_4/A-MPCF was reduced from 0.90 to 0.74, whereas the MWA performance was only slightly decreased. This work proposes a simple strategy for simultaneously adjusting MWA and EMI shielding performances of materials.



Key words: carbon foam; microwave absorption; electromagnetic interference shielding; mesophase pitch

The speedy advancement of communication technology has not only enhanced the convenience of human lives, but also filled the surrounding environment with electromagnetic waves. These waves pose a certain hazard

Received: 2025-05-16; Revised: 2025-07-04
Foundation items: Supported by the National Natural Science Foundation of China (22378181).
* Corresponding author. E-mail: gz_xu@163.com, yuanxia126@126.com.
DOI: 10.1016/S1872-5813(25)60593-7 CSTR: 32157.14.2097-213X.2025.JFCT.0135
本文的英文电子版由 Elsevier 出版社在 ScienceDirect 上出版 (http://www.sciencedirect.com/science/journal/18725813)

to our bodies and interfere with the functioning of precision instruments[1−2]. Consequently, researchers have paid widespread attention to the effective dissipation of electromagnetic waves. Currently, there are two primary methods to evaluate the ability of materials to dissipate electromagnetic waves, namely electromagnetic interference (EMI) shielding and microwave absorption (MWA)[3−4]. The MWA performance for materials is evaluated by attenuation constant (α) and impedance matching (Z_{in}/Z_0) together[5]. The α value typically correlates positively with the conductivity. Nevertheless, excessively high conductivity can generate impedance mismatch, leading to electromagnetic waves being reflected away from the material's surface. The EMI shielding effectiveness of materials (SE_T) is related to their reflection loss (SE_R), absorption loss (SE_A), and multiple reflection loss (SE_M)[6−8]. The SE_R represents how much of incident electromagnetic waves are reflected. The SE_A reflects the absorption of electromagnetic waves within the material, driven by polarization loss, magnetic resonance, or eddy current loss. The SE_M represents the multiple reflections and scattering losses of electromagnetic waves at heterogeneous interfaces or defects within the material[9]. Unlike MWA materials, materials with high conductivity usually exhibit impressive EMI shielding performance. However, this is predominantly driven by SE_R, which can generate significant secondary pollution to the space. Thus, preparing materials with excellent EMI shielding and MWA properties simultaneously poses a significant challenge and is also a long-standing objective pursued by researchers. To obtain materials with excellent MWA performance, both a good impedance matching level and a sufficiently high attenuation constant are essential[10]. A good impedance matching level can ensure that incident electromagnetic waves efficiently enter the material's interior and are subsequently dissipated. Conversely, if the impedance matching level is not ideal, electromagnetic waves will not enter into the material but will reflect back into the free space. Such materials often have a large minimum reflection loss (RL_{min}) value and are not suitable for MWA applications. Therefore, for the purpose of constructing materials with impressive MWA and EMI shielding performance, it is rational to design EMI shielding materials dominated by SE_A.

In recent years, numerous studies have demonstrated that loading magnetic components such as Fe[11], Co[12] and Ni[13] on the carbon materials can optimize the impedance matching, thereby facilitating the dissipation of electromagnetic waves in the form of SE_A. Liu et al.[14] mixed Ni/Zn ferrite with coal tar pitch to prepare composite carbon foam through foaming and carbonization process. It was illustrated that the complex permittivity and permeability of carbon foam were improved after introducing Ni/Zn ferrite. The results showed the average SE_T of the carbon foam reached 42.0 dB in the X-band and the EMI shielding mechanism was dominated by absorption. Liu et al.[1] fabricated Fe_3O_4/carbon composite foam with the EMI shielding mechanism dominated by absorption through introducing Fe_3O_4 nanoparticles on the surface of melamine-based carbon foam. The study pointed out that the excellent EMI shielding performance of Fe_3O_4/carbon foam is ascribed to the synergistic effect between the magnetic loss of Fe_3O_4 and the dielectric loss of carbon foam matrix. It was shown that the average SE_T reached 21.0 dB in the X-band when the thickness was 4.0 mm.

In addition, the nanoporous structure of the material also exerts a significant influence on its MWA and EMI shielding performance. Kim et al.[15] pointed out that the nanoporous structure can increase the transmission path of the electromagnetic waves within the material, which promotes multiple reflections and scattering, thereby enhancing the material's absorption ability for electromagnetic waves. This finding has been confirmed by many reports as well. Luo et al.[16] systematically investigated the effect of the pore structure for activated carbon (AC) on the MWA performance by adjusting the activation temperature. It was revealed that the MWA performance of AC increased with the increase of the total pore volume (v_{pore}) for AC, which was attributed to the interfacial polarization effect inspired by the hierarchical porous structure of AC. When the v_{pore} of AC reached 0.71 cm^3/g, the RL_{min} and EAB achieved −57.75 dB and 9.86 GHz, respectively.

Mesophase pitch-based carbon foam (MP-CF) is a bulk carbon material with a closed-cell structure. It possesses many advantages such as good electrical conductivity, high chemical stability, strong acid and alkali resistance, and an easily tailored pore structure. Our team used mesophase coal pitch as the raw material and tubular carbon fibers as the additive agent to fabricate MP-CF via high pressure pyrolysis. By adjusting the additive amount of tubular carbon fibers, the effective regulation of the pore cell structure, MWA and EMI shielding performance for the carbon foam was successfully achieved. The results indicated that the MWA and EMI shielding performance of the carbon foam with tubular carbon fibers were significantly enhanced. Compared with the pure MP-CF, the average SE_T of the MP-CF with the tubular carbon fiber doping amount of 9% increased from 13.54 dB to 26.52 dB. Meanwhile, Deng et al.[17] systematically investigated the effect of graphitization degree on the MWA and EMI shielding performances by varying the carbonization temperature during the preparation process of MP-CF. It was demonstrated that with an increase graphitization degree, dipole polarization decreased and the interfacial polarization enhanced. When the optimal graphitization degree is achieved, the average SE_T, RL_{min} and EAB of MP-CF attained 35.13, −16.69 dB and 3.63 GHz, respectively. In brief, the unique pore cell structure of the MP-CF endows it with significant potentials in the fields of MWA and EMI shielding. However, there are few reports on the simultaneous application of MP-CF for MWA and EMI shielding performance.

Based on the aforementioned considerations, in this

study, a mesophase coal pitch-based carbon foam (MPCF) was fabricated via high pressure pyrolysis to serve as a framework for electromagnetic wave loss. Furthermore, in order to further enhance its electromagnetic waves loss ability by increasing the probability of contact between electromagnetic waves and pore walls, the MPCF was activated by KOH to obtain an activated MPCF (A-MPCF). Subsequently, the A-MPCF was modified with Fe_3O_4 by *in situ* growing magnetic nano-Fe_3O_4 on the pore walls to improve the overall loss capability. The mechanism of electromagnetic waves loss for the three carbon foams prepared was revealed by analyzing the EMA and EMI shielding performance, as well as the structure activity relationship. The purpose of this study is to provide a simple and feasible strategy for preparing materials with excellent EMA and EMI shielding performance simultaneously.

1 Experimental

1.1 Materials

The mesophase coal pitch (MP) was purchased from China Jining Keneng New Carbon Material Technology Co., Ltd., with its property parameters detailed in Table S1. Tubular carbon fibers were prepared by carbonated medical cottons at 600 °C, and medical cottons were purchased from local pharmacies. Potassium hydroxide (KOH), hydrochloric acid (HCl), trisodium citrate ($C_6H_5Na_3O_7·2H_2O$), ferric chloride ($FeCl_3·6H_2O$), sodium acetate ($C_2H_3NaO_2·3H_2O$), ethyl alcohol (CH_3CH_2OH) and glycol ($C_2H_6O_2$) were purchased from Sinopharm Chemical Reagent Co., Ltd.

1.2 Preparation of mesophase coal pitch-based carbon foam

First, the MP was pulverized to pass 150–200 mesh using a ball mill. Then, 40 g of MP powder and 3.6 g of tubular carbon fibers were thoroughly mixed. Subsequently, the mixture was placed into an autoclave, and subjected to high pressure pyrolysis at a foaming temperature of 490 °C and a foaming pressure of 7 MPa to obtain the green carbon foam. Finally, the resultant green carbon foam was carbonized at 900 °C under a nitrogen atmosphere to obtain the mesophase coal pitch-based carbon foam (named as MPCF). The detailed preparation process of MPCF can be found in previous work[18].

1.3 Preparation of mesophase coal pitch-based activated carbon foam

The MPCF was cut into a cuboid with a dimension of 22.86 mm×10.16 mm×3.00 mm. Next, the rectangular MPCF was subjected to ultrasonic treatment in a 1.8 mol/L KOH ethanol solution for 4 h. After that, the mixture was transferred into a drying oven to evaporate the solution at 70 °C for 10 h. Subsequently, the impregnated rectangular MPCF was activated at 850 °C for 2 h in a tubular furnace under a nitrogen atmosphere. Finally, the activated sample was washed to neutrality using 0.1 mol/L HCl solution and deionized water to obtain activated MPCF (named as A-MPCF).

1.4 Preparation of Fe_3O_4/A-MPCF

A mixed solution was prepared by adding $FeCl_3·6H_2O$ (1.14 g), $C_6H_5Na_3O_7·2H_2O$ (0.72 g) and $C_2H_3NaO_2·3H_2O$ (4.00 g) into ethylene glycol (40 mL), and then stirred vigorously for 0.5 h using a magnetic stirrer. A-MPCF was placed in a hydrothermal reactor containing the mixed solution, and then the hydrothermal reactor was placed in an oven set at 220 °C to react for 6 h. After the hydrothermal reaction, the prepared carbon foam was successively washed three times with ethanol and deionized water. Finally, the washed sample was dried to obtain the Fe_3O_4 decorated A-MPCF (named as Fe_3O_4/A-MPCF). The strategy for preparation of MPCF, A-MPCF and Fe_3O_4/A-MPCF is shown in Figure 1. The characterization methods of the samples can be seen in the Support Information.

1.5 MWA and EMI shielding effectiveness measurement

1.5.1 MWA performance

The electromagnetic parameters of the carbon foams were measured by a Vector Network Analyzer (Agilent E5071C, USA) using the coaxial line method. First, the samples for testing were ground to pass 60–80 mesh. Then, the ground carbon foam powders were mixed with paraffin in a mass ratio of 7∶3 to prepare toroidal specimens (7.00 mm outer diameter, 3.04 mm inner diameter and 2.00 mm thickness). The specimens were measured in a coaxial test fixture to obtain the relative complex permittivity (ε_r) and complex permeability (μ_r) in the frequency range of 2–18 GHz. The dielectric loss tangent (tan δ_ε) and magnetic loss tangent (tan δ_μ) were calculated through the following equations:

$$\tan\delta_\varepsilon=\frac{\varepsilon''}{\varepsilon'} \quad (1)$$

$$\tan\delta_\mu=\frac{\mu''}{\mu'} \quad (2)$$

Based on the transmission-line theory, the reflection loss (*RL*) was simulated calculated using the tested ε and μ values[19–20]:

$$Z_{in}=Z_0\times\sqrt{\frac{\mu_r}{\varepsilon_r}}\times\tanh\left(j\frac{2\pi fd\sqrt{\mu_r\varepsilon_r}}{c}\right) \quad (3)$$

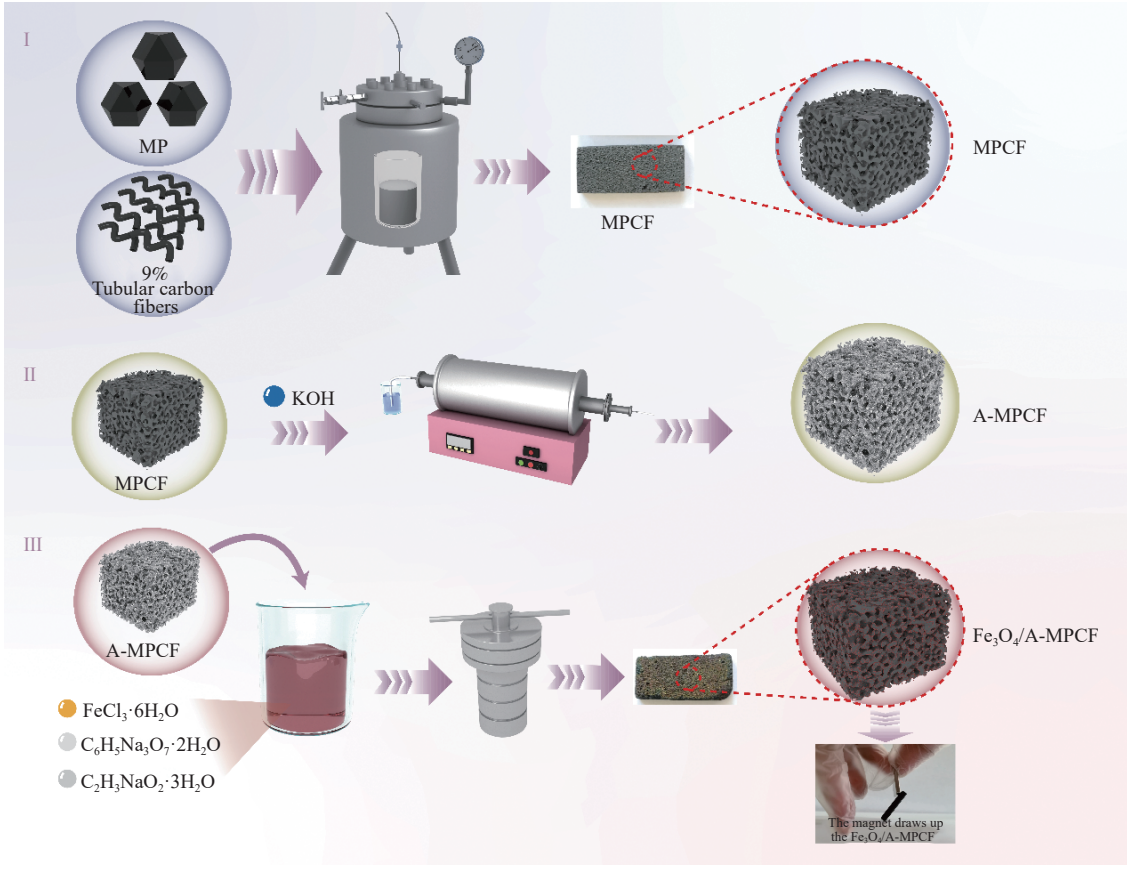


Fig. 1 Schematic diagram of the preparation for MPCF, A-MPCF and Fe_3O_4/A-MPCF

$$RL=20\lg\left|\frac{Z_{in}-Z_0}{Z_{in}+Z_0}\right| \quad (4)$$

where Z_0, Z_{in}, f, c and d are the impendence of free space, the input impendence of absorber, the frequency of microwave, the speed of light in vacuum and the coating thickness. The attenuation constant (α) was determined using following equation[21]:

$$\alpha=\frac{\sqrt{2}\pi f}{c}\times\sqrt{(\mu''\varepsilon''-\mu'\varepsilon')+\sqrt{(\mu''\varepsilon''-\mu'\varepsilon')^2+(\mu''\varepsilon''+\mu'\varepsilon')^2}} \quad (5)$$

1.5.2 EMI shielding performance

The S parameter of samples with a thickness of 3 mm was tested by a vector network analyzer (Agilent N5234A, USA) using the waveguide method in the X-band (8.2–12.4 GHz). The carbon foams were cut into 22.86 mm×10.16 mm×3.00 mm to fit the size of waveguide cavity. Absorption coefficient (A), reflection coefficient (R) and transmission coefficient (T) were calculated according to Equations (6)−(8), respectively. Absorption loss efficiency (SE_A), and reflection loss efficiency (SE_R) were calculated according to Equations (9) and (10), respectively[22–23].

$$R=|S_{11}|^2 \quad (6)$$

$$T=|S_{21}|^2 \quad (7)$$

$$A=1-R-T \quad (8)$$

$$SE_R=-10\lg(1-R) \quad (9)$$

$$SE_A=-10\lg\left(\frac{T}{1-R}\right) \quad (10)$$

When SE_A > 15 dB, the SE_M is negligible. Therefore, the SE_T of the composite material can be expressed as[14].

$$SE_T=SE_R+SE_A \quad (11)$$

2 Results and discussion

2.1 Microstructure characterization of carbon foams

The pore morphology of MPCF is very uniform, as shown in Figure 2(a), with a significant decrease in pore diameter and a sharp rise in pore number in contrast with carbon foam without added tubular carbon fibers (Figure S1). As shown in Figure 2(b), the pore size of MPCF is mainly distributed between 50–250 μm, and the pore cell density (N_{cell}, cell/cm^3), bulk density (g/cm^3), porosity (%), and average pore cell diameter (μm) are also listed in Figure 2(b). A-MPCF exhibits similar pore cell morphology to that of MPCF, as observed by comparing Figure 2(a) and (d). Additionally, numerous wrinkles are observed on the surface of the pore cells in MPCF (Figure 2(c)) and A-MPCF (Figure 2(e)).

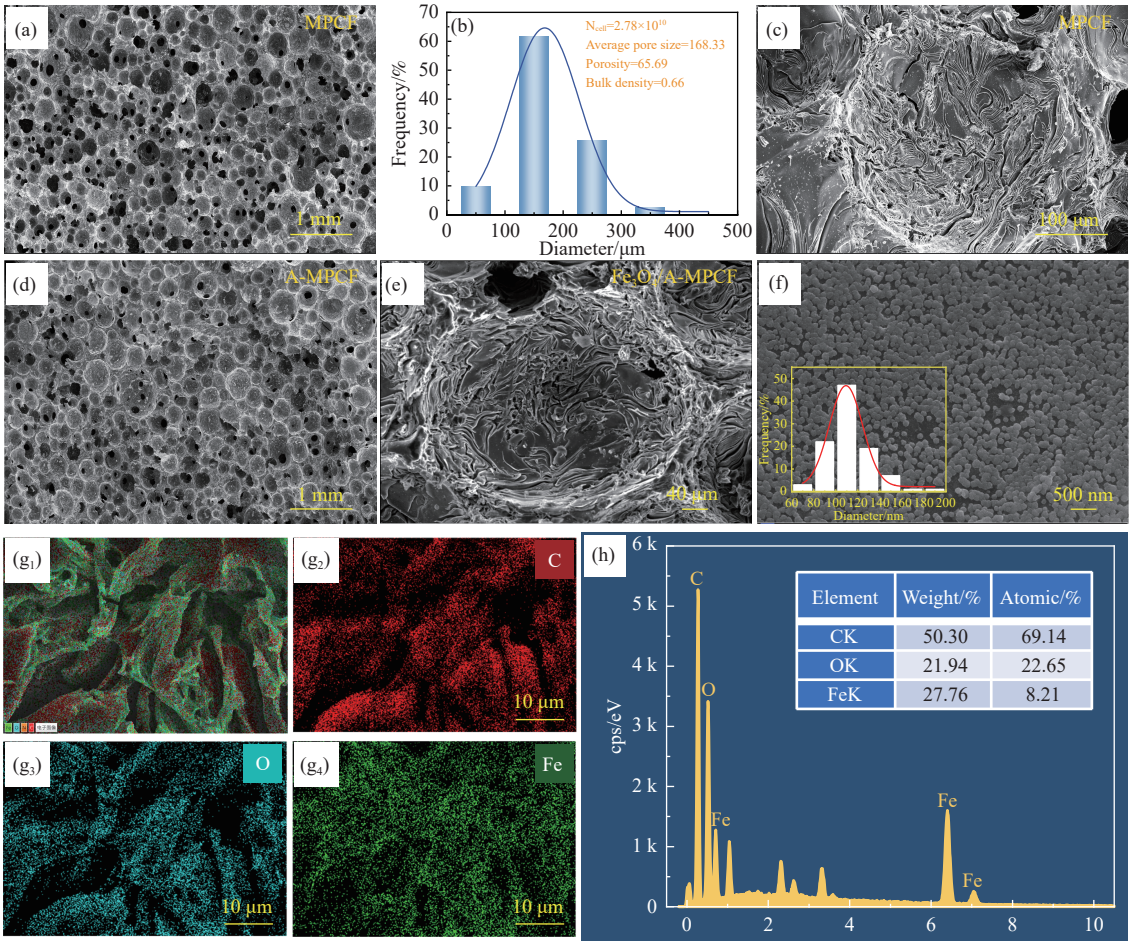


Fig. 2 (a) The SEM image of MPCF, (b) the pore cell size distribution of MPCF, (c) the enlarged SEM image of MPCF, (d) the SEM image of A-MPCF, (e) and (f) the enlarged SEM image of Fe_3O_4/A-MPCF, and the inset image is the particle size distribution of Fe_3O_4, (g) elemental mapping of Fe_3O_4/A-MPCF, (h) the EDS spectrum and elemental composition of Fe_3O_4/A-MPCF

As shown in Figure 2(e) and (f), the pore wall surface of Fe_3O_4/A-MPCF is covered by dense nanoparticles with an average diameter of 109.40 nm. It can be found from Figure 2 (g) and (h) that Fe and O elements are homogeneously dispersed on the surface of Fe_3O_4/A-MPCF, suggesting the successful loading of nano Fe_3O_4 on the A-MPCF pore surface.

The texture of three kinds of composite carbon foam (MPCF, A-MPCF and Fe_3O_4/A-MPCF) was measured using low-temperature nitrogen adsorption/desorption test. The adsorption/desorption isotherms and the pore size distributions of the samples are displayed in Figure S2 and Figure 3(a), respectively, and other textural parameters are listed in Table 1. From Figure 3(a), it can be found that two peaks of pore size distribution in 1–2 and 2–6.5 nm are displayed for A-MPCF, which is absent for MPCF and Fe_3O_4/A-MPCF. In addition, it can also be observed from Table 1 that compared to MPCF, the specific surface area (S_{BET}) of A-MPCF has increased from 2.24 to 45.96 m^2/g, micropore volume from 0 to 0.011 m^3/g, mesopore volume from 0.0080 to 0.036 m^3/g, which suggests MPCF has been successfully activated by KOH. Moreover, the S_{BET}, micropore volume and mesopore volume for Fe_3O_4/A-MPCF all have reduced in contrast with A-MPCF, which illustrates that the nano-Fe_3O_4 preferentially grows on the surfaces of highly active micropores and mesopores of A-MPCF, thereby covering both micropores and mesopores.

Subsequently, XRD tests were performed for MPCF, A-MPCF and Fe_3O_4/A-MPCF, and the results are presented in Figure 3(b). Prepared carbon foams display characteristic peaks of C (002) and (100) at approximately 26° and 43°, which are typical features of amorphous carbon[17,24]. Compared to MPCF, the (002) diffraction peak of A-MPCF is significantly wider, indicating an increase in disorder[10], which is related to the increase in the number of micropores and defects generated after activation. The XRD pattern of Fe_3O_4/A-MPCF shows characteristic diffraction peaks belonging to the (311), (400) and (440) crystal planes of Fe_3O_4 at 2θ=35.48°, 43.12° and 62.62° (PDF#97-0.15-9963), respectively.

Figure 3(c) displays the Raman spectra for carbon foams. All samples exhibit two peaks at 1350 and 1580 cm^{-1}, which correspond to the D and G bands, respectively.

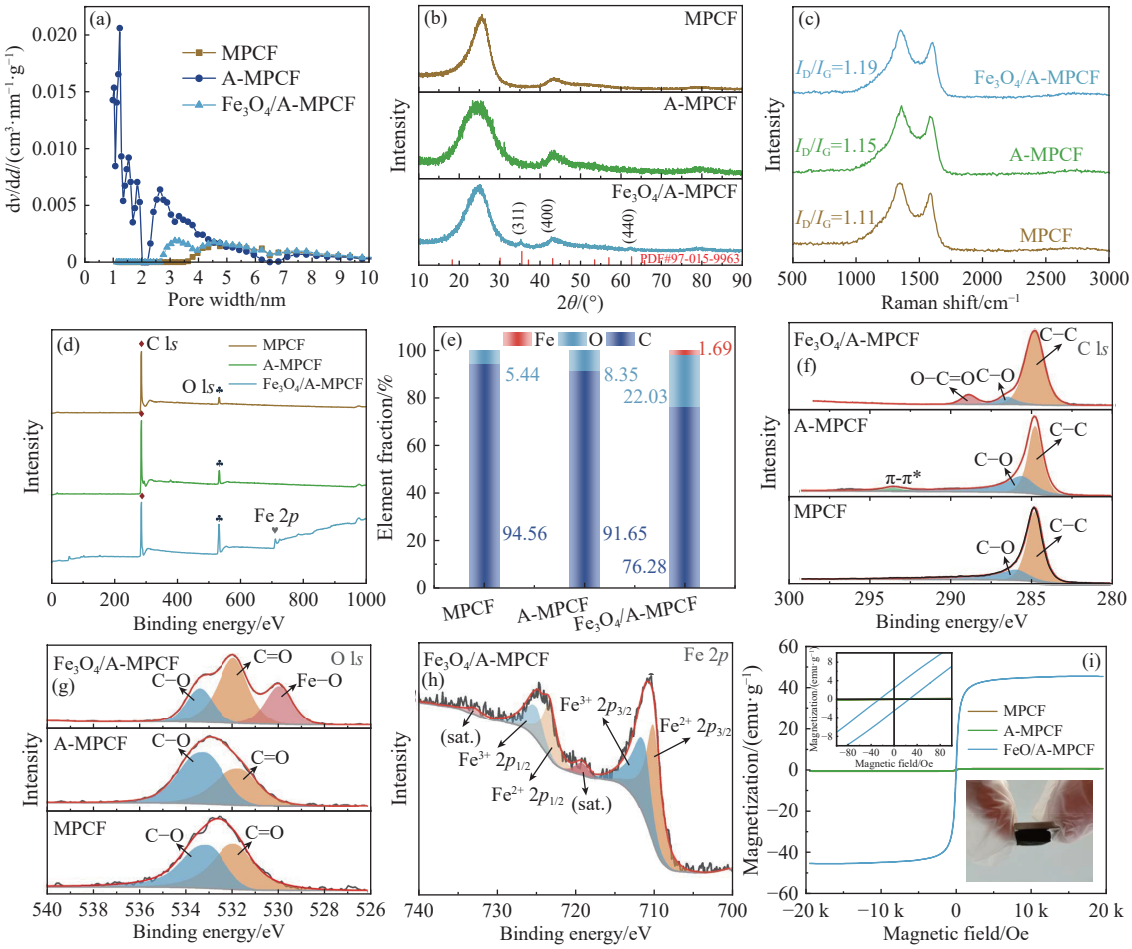


Fig. 3 (a) Pore size distributions for samples, (b) XRD patterns, (c) Raman spectra, (d) Full-scan XPS spectra of samples, (e) The elemental content of samples; high-scan XPS spectra of samples for (f) C 1*s*, (g) O 1*s* and (h) Fe 2*p*, (i) Magnetic hysteresis loops of samples

Table 1 Pore structure parameters of carbon foams prepared

Sample	S_{BET} /($m^2 \cdot g^{-1}$)	Average pore diameter /nm	Micropore volume /($cm^3 \cdot g^{-1}$)	Mesopore volume /($cm^3 \cdot g^{-1}$)	Total pore volume /($cm^3 \cdot g^{-1}$)
MPCF	2.24	33.90	0	0.0080	0.0080
A-MPCF	45.96	4.07	0.011	0.036	0.047
Fe_3O_4/A-MPCF	5.24	17.42	0	0.023	0.023

Usually, the D band refers to the defect degree in carbon materials, while the G band represents sp^2 carbon networks[25−26]. The intensity ratio of the D and G peak (I_D/I_G) serves as an indicator of the graphitization degree or defect degree[27]. Compared with that of MPCF (1.11), the I_D/I_G value of 1.15 for A-MPCF has significantly increased, indicating an increase in the disorder and defect degree of A-MPCF, which is aligned with the XRD results. After the *in situ* growth of nano-Fe_3O_4, the I_D/I_G value achieved 1.19, which suggests that the introduction of nano-Fe_3O_4 improved the defect degree of Fe_3O_4/A-MPCF. Liu et al.[28] pointed out that increasing the defect level of materials is beneficial for improving their EMW absorption and EMI shielding performance.

XPS tests were performed to analyze the surface chemical states of elements. Figure 3(d) exhibits XPS full-scan spectra for three samples. The XPS full-scan spectra of MPCF and A-MPCF present the characteristic peaks at 284.8 and 532.0 eV assigning to the C 1*s* and O 1*s*, indicating the presence of abundant C and O elements[26]. As depicted in Figure 3(e), the O element contents for A-MPCF is slightly increased, meaning that KOH activation introduces new oxygen functional groups for A-MPCF. In addition to the characteristic peak of C 1*s* and O 1*s*, the XPS full-scan spectra of Fe_3O_4/A-MPCF display the characteristic peak of Fe 2*p* (711 eV), suggesting that C, O and Fe elements coexist in Fe_3O_4/A-MPCF. As displayed in Figure 3(f), the high-resolution C 1*s* spectra of MPCF, A-MPCF and Fe_3O_4/A-MPCF each show peaks of C−C (284.80 eV) and C−O (286.54 eV)[29]. The C 1*s* spectrum of Fe_3O_4/A-MPCF exhibits the peak at 288.89 eV, corresponding to the signal of O−C=O[30]. The O 1*s* spectra

of MPCF, A-MPCF and Fe_3O_4/A-MPCF (Figure 3(g)) show characteristic peaks of C=O and C−O at 531.96 and 533.42 eV, respectively[31]. In addition, Fe_3O_4/A-MPCF shows the characteristic peak of O−Fe at 529.88 eV[32]. The high-resolution Fe 2*p* spectrum for Fe_3O_4/A-MPCF is shown in Figure 3(h), in which six characteristic peaks are observed. The peaks at 710.03 and 723.34 eV are attributed to Fe $2p_{3/2}$ and Fe $2p_{1/2}$ of Fe^{3+}, and those at 711.24 and 724.99 eV are assigned to Fe $2p_{3/2}$ and Fe $2p_{1/2}$ of Fe^{2+}, respectively[33]. The peaks at 719.25 and 732.88 eV are satellite peaks caused by shake-up excitation of high-spin oxidized Fe species. These XPS results further reveal that the ferrite in Fe_3O_4/A-MPCF exists in the form of Fe_3O_4.

Figure 3(i) shows magnetic hysteresis loops of the samples. The saturation magnetization (*Ms*) of MPCF and A-MPCF is near zero, indicating these carbon foams are non-magnetic. Fe_3O_4/A-MPCF displays a superparamagnetic behavior with the *Ms* of 45.53 emμ/g. Observing the illustration in Figure 3(i), it can be found that Fe_3O_4/A-MPCF can be instantly picked up by a magnet. These characterization results confirm that Fe_3O_4 nanoparticles have been successfully grown on the surface of A-MPCF. This is of great significance for optimizing the impedance matching level.

Figure 4 displays the conductivity of the samples. It can be found that KOH activation has little effect on the conductivity of carbon foam. Compared to MPCF and A-MPCF, the conductivity of Fe_3O_4/A-MPCF decreases significantly. This is ascribed to the fact that Fe_3O_4 is a semiconductor material with conductivity less than carbon materials, which results in the lower conductivity of Fe_3O_4/A-MPCF.

2.2 MWA performance of carbon foams

Figure 5(a)−(c) present the 3D *RL* curves of three carbon foams in the frequency of 2–18 GHz. Compared to MPCF, the RL_{min} of A-MPCF decreases from −37.34 to −48.26 dB, indicating that the nano-pores generated by the KOH activation improve the probability of incident electromagnetic waves entering the material's interior. Moreover, the MWA performance of Fe_3O_4/A-MPCF is slightly inferior to that of MPCF and A-MPCF.

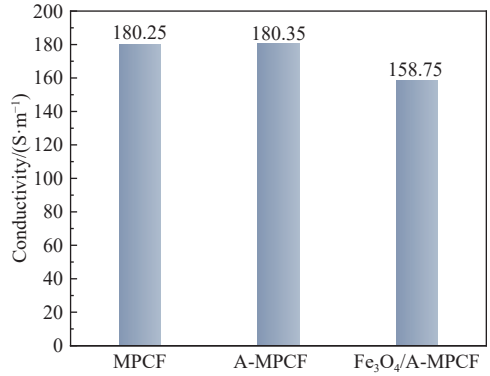


Fig. 4 The conductivity of samples

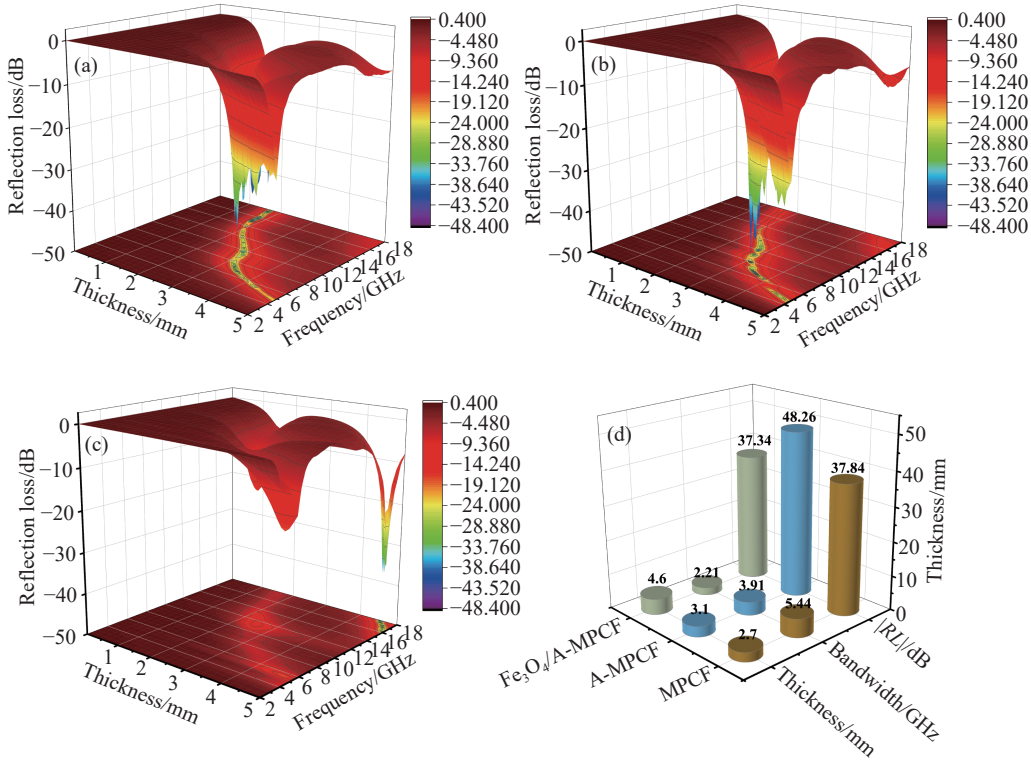


Fig. 5 3D curves of the reflection loss for (a) MPCF, (b) A-MPCF, (c) Fe_3O_4/A-MPCF, (d) 3D histogram of $|RL_{min}|$, coating thickness and EAB

The reason may be that the introduction of nano-Fe_3O_4 endows magnetism for Fe_3O_4/A-MPCF, while reduces its conductivity (Figure 4), leading to the weakened dielectric loss ability. To evaluate the MWA performance of the samples, a 3D column graph containing $|RL_{min}|$, *EAB*, and coating thickness was presented in Figure 5(d). Compared to other similar MWA materials, A-MPCF achieves the RL_{min} of −48.26 dB and an *EAB* of 3.91 GHz at a coating thickness of 3.1 mm.

Generally, the MWA performance of materials correlates closely with the relative complex permittivity and permeability[34−35]. The complex permittivity includes the real part (ε') and the imaginary part (ε''), and the complex permeability contains the real part (μ') and the imaginary part (μ''). The real part and imaginary part respectively represent the storage capacity and loss capacity to the electromagnetic wave for the absorbents[36−37]. Materials with higher conductivity and saturation magnetization exhibit enhanced dielectric and magnetic loss capabilities. Figure 6(a) and (b) show the complex permittivity of samples. As frequency increases, both the ε' and ε'' of samples exhibit a downward trend. This is commonly associated with the delayed response of dipole polarization to potential changes in the GHz range[38]. All samples have multiple resonance peaks in the frequency range of 2–18 GHz, indicating that the prepared carbon foams display multiple polarization loss behaviors. As shown in Figure 6(c), the variation trend of dielectric loss angle tangent (tan δ_ε) is essentially in line with that of ε'' for samples. Among them, the tan δ_ε value of Fe_3O_4/A-MPCF is always lower than that of others, confirming that Fe_3O_4/A-MPCF has the poor dielectric loss capacity. Figure 6(d) and (e) display the complex permeability for carbon foams. The μ' of MPCF and A-MPCF are close to 1, while μ'' are about 0, indicating that MPCF and A-MPCF are not magnetic. While there are multiple formants for Fe_3O_4/A-MPCF, this indicates the existence of magnetic resonance loss[39].

In addition, the value of μ' and μ'' for Fe_3O_4/A-MPCF show an increasing trend in the high frequency range. Recent studies have established that the applied electromagnetic field can make the composite electrically polarized and magnetically polarized simultaneously, thus forming electromagnetic coupling and improving the complex permeability of the composite at the high frequency region[40]. The μ'' value of three samples is negative in several frequency region. This phenomenon may be attributed to the phase lag between the capacitor and the inductor on the porous structure[28]. Furthermore, the value of tan δ_μ can reflect the magnetic energy dissipation of the material. Figure 6(f) reveals that tan δ_μ exhibits little difference among materials in the high frequency region. However, the tan δ_μ of Fe_3O_4/A-MPCF in the low frequency region is significantly higher than that of the other two materials, meaning that it exhibits the strongest magnetic loss capacity. Finally, the tan δ_ε values for all samples are significantly higher than tan δ_μ, indicating that dielectric loss is the dominant attenuation mechanism.

For the other hand, it has been widely accepted that the magnetic loss mechanisms in MWA materials mainly consist of hysteresis loss, eddy current loss, domain wall loss, and natural resonance[41]. The hysteresis loss primarily occurs near 100 MHz, rather than in the microwave frequency range. Meanwhile, the domain wall loss occurs only in multi-domain structured materials[42]. Thus, in the GHz frequency range, natural resonance and eddy current loss dominate the loss mechanisms for Fe_3O_4/A-MPCF. The eddy current loss value (C_0) can be described by Equation (12).

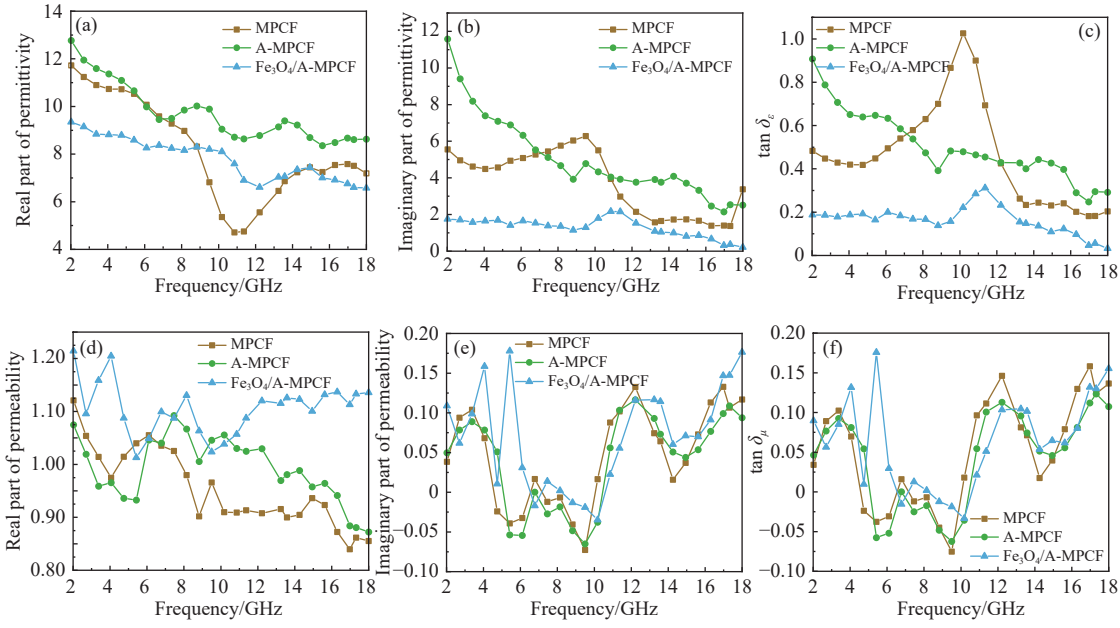


Fig. 6 (a) the real and (b) imaginary part of complex permittivity, (c) and tangent of dielectric loss angle for samples, (d) the real and (e) imaginary part of complex permeability, (f) tangent of magnetic loss angle for samples

$$C_0=\mu''(\mu')^{-2}f^{-1} \quad (12)$$

If the eddy current loss is the sole attenuation mechanism, the C_0 value does not change with the frequency variation[43]. As presented in Figure 7(a), the C_0 values of Fe_3O_4/A-MPCF vary with frequency, indicating that the eddy current loss plays a very limited role. Consequently, the dominant mechanism of magnetic loss in Fe_3O_4/A-MPCF is natural resonance.

The dielectric loss primarily includes the polarization relaxation and conduction loss. The polarization relaxation primarily consists of the electron, ion, dipole, and interface polarization. However, the electron and ion polarization typically occur in the THz and PHz frequency ranges. Therefore, in the GHz frequency range, the polarization relaxation primarily results from the dipole and interface polarization[44]. Generally, Debye theory is commonly employed to analyze the dielectric relaxation process[45]. Based on Debye theory, the relationship between the ε' and ε'' is expressed by Equation (13):

$$\left(\varepsilon'-\frac{\varepsilon_s+\varepsilon_\infty}{2}\right)^2+(\varepsilon'')^2=\left(\frac{\varepsilon_s-\varepsilon_\infty}{2}\right)^2 \quad (13)$$

where ε_s represents the static permittivity, and ε_∞ represents the relative permittivity at high-frequency limit. The curve of ε' *vs.* ε'' is known as the Cole-Cole curve, where each semicircle indicates the presence of a Debye relaxation process. From Figure 7(b)–(d), multiple semicircles exist in all carbon foams, showing that they exhibit multiple Debye relaxation processes, which means that all samples display multiple polarization loss behaviors. In addition, the Cole-Cole curves of all samples show a straight line at the tail, which suggests that all carbon foams dissipate electromagnetic wave in the form of conduction loss[32].

Figure 8(a)–(c) display the characteristic impedance matching (Z_{in}/Z_0) curves of samples, and Figure 8(d) shows the corresponding attenuation constant (α) curves. When the Z_{in}/Z_0 value approaches 1, it indicates that most electromagnetic waves are incident inside the material[46]. A higher α value facilitates the dissipation of electromagnetic waves within the material. Fe_3O_4/A-MPCF has the best impedance matching level, but it has the lowest α value. MPCF shows the highest α value, but its impedance matching level is poor. By contrast, the α value and impedance matching level of A-MPCF are in the middle level.

As shown in Figure 4(d), the RL_{min} of Fe_3O_4/A-MPCF (−37.34 dB) and MPCF (−37.84 dB) are very close, while A-MPCF exhibits the optimal RL_{min} (−48.26 dB). This highlights the importance of balancing impedance matching and attenuation constant to achieve optimal MWA performance.

Based on the above, the differences in the MWA performance of the prepared carbon foams are primarily attributed to the following reasons: After KOH activation, the S_{BET} of A-MPCF significantly increases compared to that of MPCF, rising from 2.24 to 45.96 m^2/g. This increase means the generation of abundant nanopores on the pore cell walls of A-MPCF.

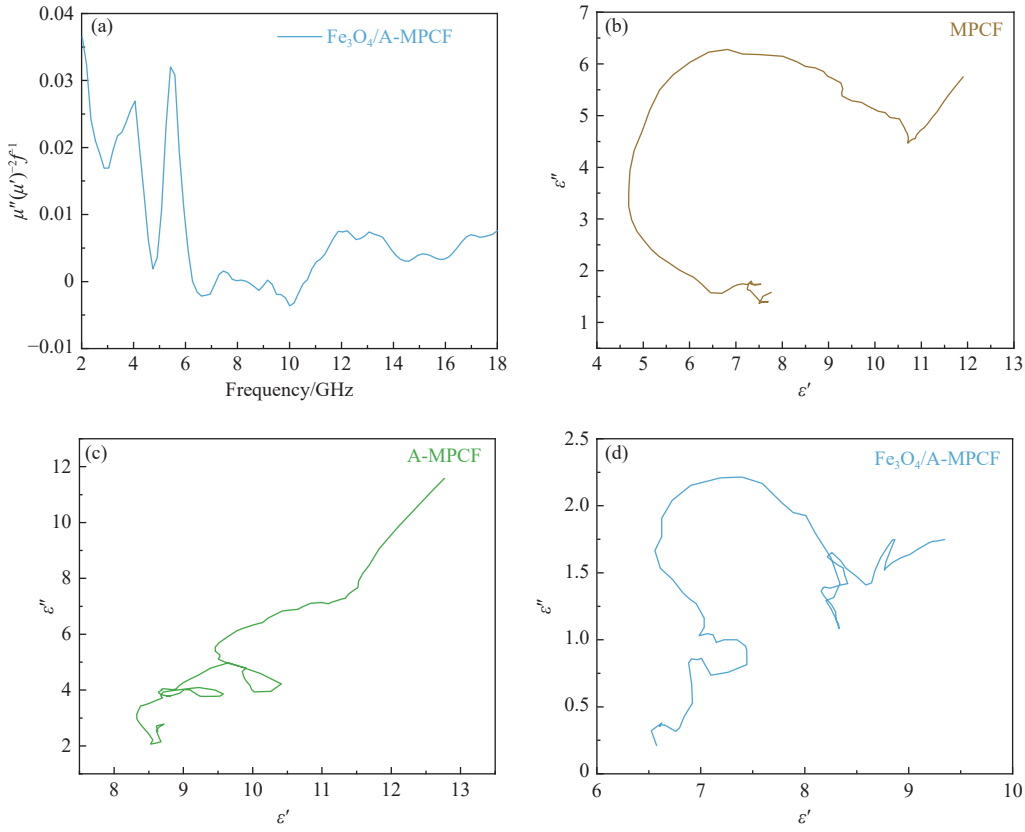


Fig. 7 (a) $\mu''(\mu')^{-2}f^{-1}$ of the Fe_3O_4/A-MPCF, (b)–(d) Cole-Cole curve of the samples

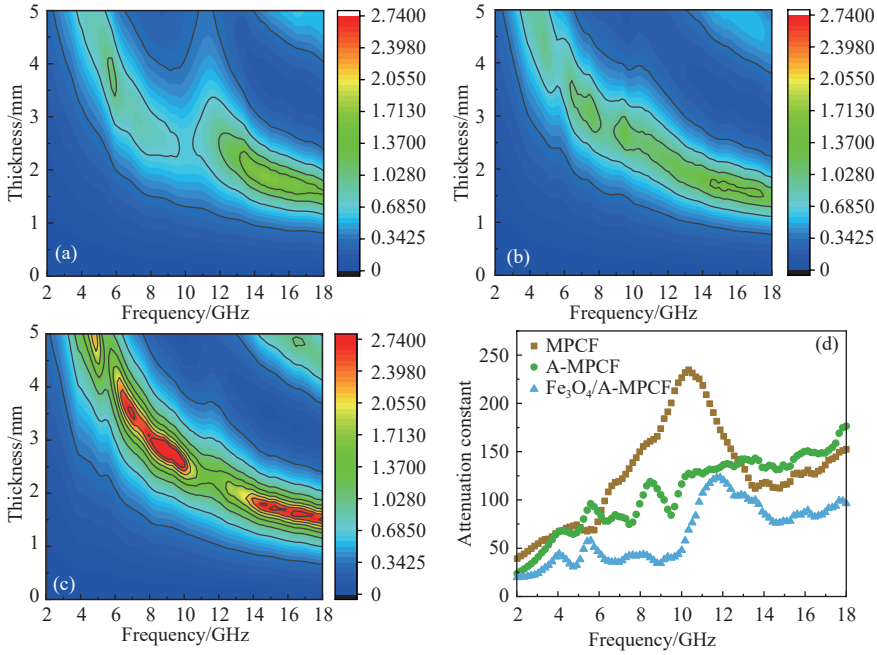


Fig. 8 Impedance matching horizontal contour plots of carbon foams (a) MPCF, (b) A-MPCF, (c) Fe_3O_4/A-MPCF, (d) attenuation constant

When electromagnetic waves are incident on the pore cell walls of A-MPCF, these nanopores increase the number of reflections and diffuse reflections within A-MPCF. This enhances the interaction between electromagnetic waves and A-MPCF, resulting in greater energy absorption and dissipation, thereby improving the MWA performance of A-MPCF. However, the specific surface area results show that the BET value of Fe_3O_4/A-MPCF obviously decreases from 45.96 to 5.24 m^2/g after the introduction of Fe_3O_4. This indicates that the Fe_3O_4 nanoparticles have blocked the partial nanopores of the A-MPCF matrix. In addition, the conductivity test results demonstrate that the conductivity of Fe_3O_4/A-MPCF reduces from 180.35 to 158.75 S/m. These results suggest that the introduction of Fe_3O_4 nanoparticles endows Fe_3O_4/A-MPCF with magnetic loss ability, it also decreases the probability of electromagnetic wave reflection and scattering within the Fe_3O_4/A-MPCF, and weakens its conduction loss ability. Therefore, the impedance matching of Fe_3O_4/A-MPCF is improved, while its MWA performance is diminished. Consequently, based on the aforementioned discussion and the results of MWA performance test, we conclude that A-MPCF exhibits the optimal MWA performance.

2.3 EMI shielding performance

Figure 9(a) and (b) respectively present the SE_T curves and the average values of SE_A, SE_R and SE_T for the samples. All samples exhibit certain EMI shielding performance. Notably, the average SE_T of A-MPCF and Fe_3O_4/A-MPCF reaches 103.0 and 96.9 dB, respectively, significantly outperforming most EMI shielding materials reported in previous studies (see Table 2 for comparison). The A-MPCF exhibits the optimal average SE_T, which can be attributed to its unique three-dimensional hierarchical porous structure. This structure effectively extends the transmission path of electromagnetic waves, thereby enhancing the structural loss ability of A-MPCF. Consequently, the EMI shielding performance of A-MPCF is significantly improved. For Fe_3O_4/A-MPCF, although its magnetic loss capability for electromagnetic waves is enhanced, its structural and conductive loss capabilities are somewhat reduced, which in turn leads to a slight decrease in its average SE_T.

T, R and A of carbon foams are depicted in Figure 9(c). The T values of all materials are near zero, suggesting that almost no electromagnetic waves pass through the materials. Although R values of all materials are greater than their A values, which does not prove that the primary loss mechanism for electromagnetic waves is surface reflection. This is because the R value includes power reflected from the foam material's outer surface, as well as multiple reflections and scattering from its interior[47]. Among them, Fe_3O_4/A-MPCF has the lowest R value, which mainly attributed to two factors: (1) The introduction of Fe_3O_4 nanoparticles can optimize the impedance matching level, reducing electromagnetic waves reflected from the surface of A-MPCF; (2) nano Fe_3O_4 causes the blockage in micropores for A-MPCF, resulting in a reduction of the multiple reflection and scattering of electromagnetic waves within Fe_3O_4/A-MPCF. Based on the above discussion, it is concluded that the Fe_3O_4/A-MPCFpossesses the optimal EMI shielding performance.

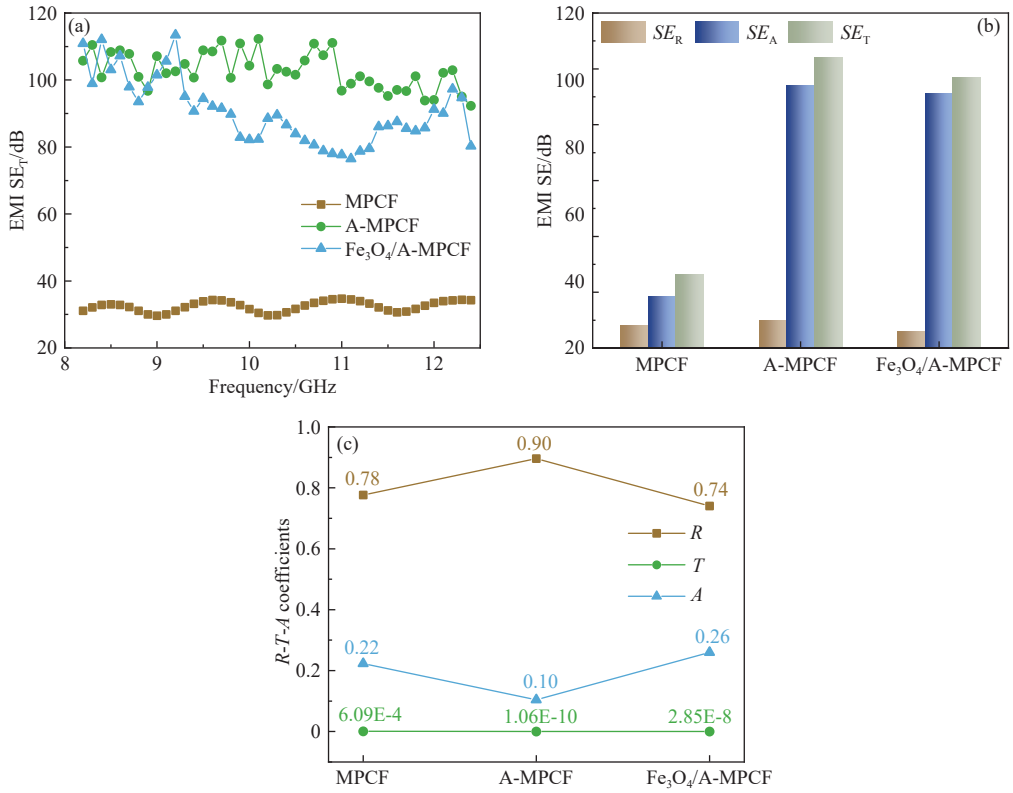


Fig. 9 (a) The SE_T curves, (b) the average value of SE_T, SE_A and SE_R, (c) R, A and T coefficients of samples

2.4 Analysis of electromagnetic wave dissipation mechanism

Electromagnetic waves dissipation mechanism for Fe_3O_4/A-MPCF is shown in Figure 10. It is mainly attributed to the following aspects:

(1) When electromagnetic waves enter the 3D interconnected pore structure, they will be reflected and scattered on the pore cell wall for many times.

(2) Electromagnetic waves react with the electron carrier on the conductive network, converting the electromagnetic waves into heat energy by induced micro-current (i.e., conduction loss).

(3) The abundant defects can serve as the polarization centers, triggers the dipole moment imbalance and dipole polarization, effectively dissipating incident electromagnetic waves under alternating electromagnetic fields.

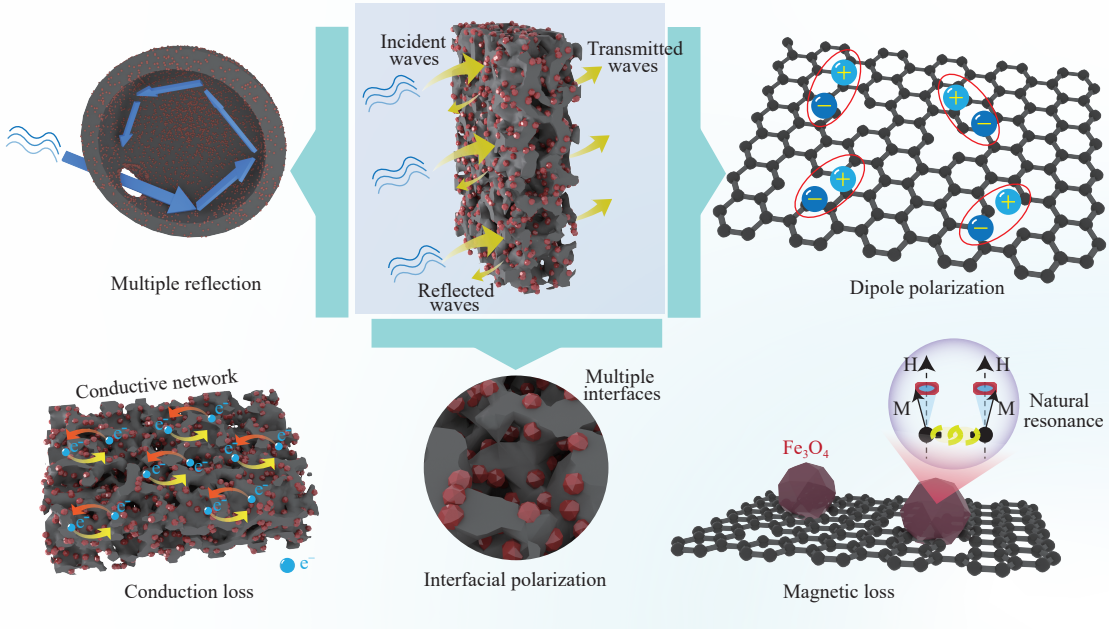


Fig. 10 Electromagnetic wave loss mechanism of Fe_3O_4/A-MPCF

(4) There are rich heterogeneous interfaces (Fe_3O_4, MP carbon and hollow carbon fiber) in Fe_3O_4/A-MPCF. Accumulation of the space charge at the heterogeneous interface boundary creates a capacitor-likely structure, which attenuates the power of the incident electromagnetic waves through the arrangement of charges or polar bonds, resulting in the interface polarization loss.

(5) A large number of nano Fe_3O_4 can be used as magnetic loss centers to attenuate electromagnetic waves, and the loss mechanism can be attributed to natural resonance (Figure 7(a)).

In brief, the loss mechanism of Fe_3O_4/A-MPCF to electromagnetic waves is the synergistic effect of the conduction loss, multiple reflection and scattering, dipole polarization, interface polarization, and natural resonance, in which the multiple reflections and scattering as well as the dipole polarization are the main electromagnetic wave loss mechanisms for Fe_3O_4/A-MPCF.

To objectively evaluate the MWA and EMI shielding performances of prepared carbon foams, the MWA and EMI shielding performances of the carbon foams prepared in this work were compared with those of the reported materials, as shown in Table 2.

Table 2 Comparison of MWA and EMI shielding performances for the currently reported materials

Sample	RL_{min}/dB	*EAB*/GHz	Average SE_T/dB	Ref.
CCF-Fe_3O_4	−56.8	7.1	—	[33]
PANI@MoS_2	−49.7	4.3	—	[5]
FeCo/ZnO	−34.8	5.1	—	[48]
CoO/CF	−14.1	2.1	—	[12]
$MoO_3/TiO_2/Mo_2TiC_2T_x$	−30.76	8.6	—	[49]
SiO_2@$Ti_3C_2T_x$@CoNi	−63.95	4.56	—	[50]
AC-600 (1:1)	−37	8.8	—	[51]
CF-700	−16.69	3.63	—	[17]
Fe_7/Co_3	−53.6	6.8	—	[35]
PANI/Fe_3O_4/MWCNTs	−16	7.0	—	[36]
CDC/Ni	−32	2.16	—	[37]
CoFe-alloy/C	−60	7.64	—	[38]
NRGO/hollow $CoFe_2O_4$	−30.8	7.04	—	[32]
PI@CNCs/CF	−60.5	10.8	—	[52]
CF/CNCs-2	−64.6	9.0	—	[53]
$Ti_3C_2T_x$@polyaniline/MWCNT	−54.7	6.0	—	[54]
Bagasse fiber/PANI	—	—	28.8	[55]
CNTs/MCF/Fe_3O_4	—	—	46.41	[56]
Peanut shell/hazelnut shell	—	—	6	[57]
PEDOT:PSS/Fe_3O_4-NG/CP	—	—	54	[58]
*r*GO@Fe_3O_4/CNT/T-ZnO@Ag/WPU	—	—	92.3	[59]
PCPES-30%/Cu	—	—	59.7	[3]
c-MG/PA	—	—	49	[60]
$Ti_3C_2T_x/Fe_3O_4$&BC/Fe_3O_4&MTMS	—	—	68	[61]
PEDOT/wood	—	—	46.2	[62]
CNT/PLA	—	—	47.1	[63]
$FeCl_3$/CNTs/PVP/PU	—	—	91.5	[64]
$Ti_3C_2T_x$/GO	—	—	51.4	[65]
MPCF	−37.84	5.44	26.52	this work
A-MPCF	−48.26	3.91	103	this work
Fe_3O_4/A-MPCF	−37.34	2.21	96.93	this work

3 Conclusions

In conclusion, three kinds of mesophase pitch-based carbon foams were successfully prepared by high-pressure pyrolysis, KOH activation and hydrothermal methods. The KOH activation provides a unique pore structure for the carbon foam, that is, there are 3D connected micron sized pore cells and abundant micropores on the pore walls. This unique pore structure optimizes the impedance matching level, and also enhances the dielectric loss capacity of the activated carbon foam, thereby improving the electromagnetic wave loss capacity. The MWA test results show that A-MPCF exhibits the best MWA performance, with the RL_{min} of −48.26 dB at a coating thickness of 3.1 mm and an EAB of 3.91 GHz. Subsequently, the introduction of

nano Fe_3O_4 endows the composite carbon foam with magnetic loss capability. Compared to A-MPCF, the MWA performance of Fe_3O_4/A-MPCF slightly decreases. However, the R value of Fe_3O_4/A-MPCF notably reduces from 0.90 to 0.74. When the thickness of Fe_3O_4/A-MPCF is 4.6 mm, its RL_{min} achieves −37.34 dB with an EAB of 2.21 GHz. The average SE_T of Fe_3O_4/A-MPCF with the thickness of 3.0 mm achieves 96.93 dB in X-band, which is superior to the EMI shielding performance of materials reported in the literature. This work proposes a simple strategy for simultaneously adjusting MWA and EMI shielding performances of MWA materials.

Declaration of Competing Interest

The authors declare no conflict of interest.

References

[1] LIU H, WU S, YOU C, et al. Fe_3O_4 nanoparticles decorated flexible carbon foam for efficient electromagnetic interference shielding[J]. Ceram Int, 2022, 48(13): 19452−19459.

[2] DAI Z, WEI Y, HU C, et al. Effects of pore structure on wide-frequency electromagnetic interference shielding performance of carbonized wood[J]. Compos Commun, 2023, 38: 101501.

[3] ZHAO H, HUANG Y, HAN Y, et al. Flexible and lightweight porous polyether sulfone/Cu composite film with bidirectional differential structure for electromagnetic interference shielding and heat conduction[J]. Chem Eng J, 2022, 440: 135919.

[4] LI Q, TAN J, WU Z, et al. Hierarchical magnetic-dielectric synergistic Co/CoO/RGO microspheres with excellent microwave absorption performance covering the whole X band[J]. Carbon, 2023, 201: 150−160.

[5] ZHANG W, ZHANG X, ZHENG Y, et al. Preparation of polyaniline@MoS_2@Fe_3O_4 nanowires with a wide band and small thickness toward enhancement in microwave absorption[J]. ACS Appl Nano Mater, 2018, 1(10): 5865−5875.

[6] WASEEM M, ZHANG X, WANG W, et al. Lightweight and high EMI shielding performed ZrB_2-SiC/CF@Epoxy-Fe_3O_4 composites with carbonated cotton fibers[J]. J Alloys Compd, 2025, 1030: 180915.

[7] GANGWAR S, KAR K K, AKHTAR M J. Human hair-derived carbon for flexible, lightweight EMI shielding composites[J]. Diamond Relat Mater, 2025, 157: 112540.

[8] MANOGARAN R, MURUGESAN M. A review on recent advancements in textile fabrics for electromagnetic interference (EMI) shielding materials[J]. Mater Today Commun, 2025, 44: 111879.

[9] WU N, HU Q, WEI R, et al. Review on the electromagnetic interference shielding properties of carbon based materials and their novel composites: Recent progress, challenges and prospects[J]. Carbon, 2021, 176: 88−105.

[10] WANG X, LU Y, ZHU T, et al. $CoFe_2O_4$/N-doped reduced graphene oxide aerogels for high-performance microwave absorption[J]. Chem Eng J, 2020, 388: 124317−124317.

[11] LIU X, LIU J, WU L, et al. One-pot synthesis of TiO_2–Fe_3O_4 bimetallic oxides decorated on carbon nanosheets as an efficient photothermal microwave absorber[J]. Carbon, 2025, 233: 119876.

[12] CHEN H, ZHU Y, YAN X, et al. Porous CoO/carbon foam composites synthesized by solvothermal method for supercapacitor and enhanced microwave absorption applications[J]. Diamond Relat Mater, 2023, 138: 110270.

[13] WU L, LIU J, LIU X, et al. Microwave-absorbing foams with adjustable absorption frequency and structural coloration[J]. Nano Lett, 2024, 24(11): 3369−3377.

[14] LIU H, WU J, ZHUANG Q, et al. Preparation and the electromagnetic interference shielding in the X-band of carbon foams with Ni-Zn ferrite additive[J]. J Eur Ceram Soc, 2016, 36(16): 3939−3946.

[15] KIM H H, KIM B-J. Effects of pore structure on the electromagnetic shielding characteristics of porous carbon fibers derived from various precursors[J]. Carbon, 2025, 238: 120227.

[16] LUO J, DAI Z, FENG M, et al. Hierarchically porous carbon derived from natural Porphyra for excellent electromagnetic wave absorption[J]. J Mater Sci Technol, 2022, 129(34): 206−214.

[17] DENG W, LI T, LI H, et al. Controllable graphitization degree of carbon foam bulk toward electromagnetic wave attenuation loss behavior[J]. J Colloid Interface Sci, 2022, 618: 129−140.

[18] WANG Y, XU G, GE Y, et al. MP/tubular-CF composite carbon foam of high microwave absorption and electromagnetic interference shielding properties[J]. Diamond Relat Mater, 2024, 141: 110633.

[19] PRAVEEN N, ASHISH G, MANDEEP S, et al. Excellent microwave absorbing and electromagnetic shielding performance of grown MWCNT on activated carbon bifunctional composite[J]. Carbon, 2022, 198: 151−161.

[20] LIU J, YANG Z, YANG L, et al. Rational design of yolk-shell $NiCo_2O_4$@void@$NiCo_2S_4$ nanospheres for effective enhancement in microwave absorption[J]. J Alloys Compd, 2021, 853: 157403.

[21] GU W, SHENG J, HUANG Q, et al. Environmentally friendly and multifunctional shaddock peel-based carbon aerogel for thermal-insulation and microwave absorption[J]. Nanomicro Lett, 2021, 13(1): 102.

[22] SINGH K, BAHETI V. EMI shielding and joule heating applications of woven and nonwoven activated carbon fabrics of Kevlar fibres[J]. J Anal Appl Pyrolysis, 2025, 188: 107041.

[23] JI Y, JANG J M, KIM J Y, et al. SWCNT/MWCNT binderless hybrid hydrogel: Towards large-scale high-performance EMI shielding coating at commercial level[J]. Carbon, 2025, 238: 120250.

[24] GE Y, WANG Y, XU G, et al. Biomass activated carbon supported Keggin-type polyoxometalate as an electrode material for high-performance acidic aqueous supercapacitors[J]. J Electroanal Chem, 2023, 947: 117779.

[25] WANG Y, LI M, ZHAO Z, et al. Preliminary exploration of the mechanism governing the cell structure variation of mesophase coal pitch/carbon black composite carbon foam[J]. Diamond Relat Mater, 2023, 136: 110077.

[26] GE Y, XU G, WANG Y, et al. A rigid free-standing supercapacitor electrode material made from fat coal-based activated carbon foam[J]. Chem Eng J, 2024, 491: 151553.

[27] SONG L, ZHANG F, CHEN Y, et al. Multifunctional SiC@SiO_2 nanofiber aerogel with ultrabroadband electromagnetic wave absorption[J]. Nanomicro Lett, 2022, 14(1): 152.

[28] LIU X, ZHOU J, XUE Y, et al. Structural engineering of hierarchical magnetic/carbon nanocomposites via in situ growth for high-efficient electromagnetic wave absorption[J]. Nano-Micro Lett, 2024, 16: 174.
[29] ZHAO Y, ZHU L, LI W, et al. Insights into enhanced adsorptive removal of Rhodamine B by different chemically modified garlic peels: Comparison, kinetics, isotherms, thermodynamics and mechanism[J]. J Mol Liq, 2019, 293: 111516.
[30] GE Y, WANG Y, XU G, et al. Preparation of activated carbon from soybean straw for high-efficiency adsorption methylene blue in aqueous solution[J]. Water Air Soil Poll, 2023, 234(2): 74.
[31] WALCZYK M, ŚWIĄTKOWSKI A, PAKUŁA M, et al. Electrochemical studies of the interaction between a modified activated carbon surface and heavy metal ions[J]. J Appl Electrochem, 2005, 35(2): 123−130.
[32] XU J, SHU R, WAN Z, et al. Construction of three-dimensional hierarchical porous nitrogen-doped reduced graphene oxide/hollow cobalt ferrite composite aerogels toward highly efficient electromagnetic wave absorption[J]. J Mater Sci Technol, 2023, 132: 193−200.
[33] BANDARU S, MURTHY N, KULKARNI R, et al. Magnetic ferrite/carbonized cotton fiber composites for improving electromagnetic absorption properties at gigahertz frequencies[J]. J Mater Sci Technol, 2021, 86: 127−138.
[34] JIA X, SHEN B, ZHANG L, et al. Construction of compressible polymer/MXene composite foams for high-performance absorption-dominated electromagnetic shielding with ultra-low reflectivity[J]. Carbon, 2021, 173: 932−940.
[35] CHENG Y, JI G, LI Z, et al. Facile synthesis of FeCo alloys with excellent microwave absorption in the whole Ku-band: Effect of Fe/Co atomic ratio[J]. J Alloys Compd, 2017, 704: 289−295.
[36] CAO M S, YANG J, SONG W L, et al. Ferroferric oxide/multiwalled carbon nanotube vs polyaniline/ferroferric oxide/multiwalled carbon nanotube multiheterostructures for highly effective microwave absorption[J]. ACS Appl Mater Interfaces, 2012, 4(12): 6949−6956.
[37] ZHONG L, HONGYAN L, TONGPAN Y, et al. What is the important factor affecting microwave absorption performance in corncob-derived carbon/Ni composites?[J]. J Phys D Appl Phys, 2021, 54(36): 365005.
[38] JIAO Y, DAI Z, FENG M, et al. Electromagnetic absorption behavior regulation in bimetallic polyphthalocyanine derived CoFe-alloy/C 0D/2D nanocomposites[J]. Mater Today Phys, 2023, 33.
[39] XIE A, MA Z, XIONG Z, et al. Conjugate ferrocene polymer derived magnetic Fe/C nanocomposites for electromagnetic absorption application[J]. J Mater Sci Technol, 2024, 175: 125−131.
[40] WANG K, ZHANG S, CHU W, et al. Tailoring conductive network nanostructures of ZIF-derived cobalt-decorated N-doped graphene/carbon nanotubes for microwave absorption applications[J]. J Colloid Interface Sci, 2021, 591: 463−473.
[41] ZHANG S, ZHANG F, XIE Y, et al. Ultrathin CoNi@$Ti_3C_2T_x$ composites with sandwich structures for efficient microwave absorption[J]. Ceram Int, 2022, 48(22): 33751−33762.
[42] WANG G Z, GAO Z, TANG S W, et al. Microwave absorption properties of carbon nanocoils coated with highly controlled magnetic materials by atomic layer deposition[J]. ACS Nano, 2012, 6(12): 11009−11017.
[43] WANG X, SHI G, SHI F-N, et al. Synthesis of hierarchical cobalt dendrites based on nanoflake self-assembly and their microwave absorption properties[J]. RSC Adv, 2016, 6(47): 40844−40853.
[44] WANG H Y, MA H B. Highly enhanced electromagnetic wave absorption bandwidth based on reduced graphene oxide-Fe aerogel composites[J]. Nanotechnology, 2020, 31(9): 095711.
[45] TAO J, ZHOU J, YAO Z, et al. Multi-shell hollow porous carbon nanoparticles with excellent microwave absorption properties[J]. Carbon, 2021, 172: 542−555.
[46] WU L, GAO H, GUO R, et al. MnO_2 Intercalation-guided impedance tuning of carbon/polypyrrole double conductive layers for electromagnetic wave absorption[J]. Chem Eng J, 2023, 460: 141749.
[47] AL-SALEH M H, SUNDARARAJ U. Electromagnetic interference shielding mechanisms of CNT/polymer composites[J]. Carbon, 2009, 47(7): 1738−1746.
[48] BAO X, WANG X, ZHOU X, et al. Excellent microwave absorption of FeCo/ZnO composites with defects in ZnO for regulating the impedance matching[J]. J Alloys Compd, 2018, 769: 512−520.
[49] HU F, ZHANG F, WANG X, et al. Ultrabroad band microwave absorption from hierarchical $MoO_3/TiO_2/Mo_2TiC_2T_x$ hybrids via annealing treatment[J]. J Adv Ceram, 2022, 11(9): 1466−1478.
[50] NIU H, JIANG X, XIA Y, et al. Construction of hydrangea-like core-shell SiO_2@$Ti_3C_2T_x$@CoNi microspheres for tunable electromagnetic wave absorbers[J]. J Adv Ceram, 2023, 12(4): 711−723.
[51] ADNAN A M, WEI D, SAJID U R, et al. Low cost 3D bio-carbon foams obtained from wheat straw with broadened bandwidth electromagnetic wave absorption performance[J]. Appl Surf Sci, 2021, 543: 148785.
[52] LIU X, WU L, LIU J, et al. Dynamically frequency-tunable and environmentally stable microwave absorbers[J]. Carbon Energy, 2024, 6(10): e589.
[53] WU L, SHI S, WANG G, et al. Carbon nanocoils/carbon foam as the dynamically frequency-tunable microwave absorbers with an ultrawide tuning range and absorption bandwidth[J]. Adv Funct Mater, 2022, 32(52): 2209898.
[54] FANG Y S, YUAN J, LIU T T, et al. Clipping electron transport and polarization relaxation of $Ti_3C_2T_x$ based nanocomposites towards multifunction[J]. Carbon, 2023, 201: 371−380.
[55] ZHANG Y, QIU M, YU Y, et al. A novel polyaniline-coated bagasse fiber composite with core-shell heterostructure provides effective electromagnetic shielding performance[J]. ACS Appl Mater Interfaces, 2017, 9(1): 809−818.
[56] JIN W, WANG W, MAZUMDAR S, et al. Carbon foams with Fe-organic network-derived Fe_3O_4 for efficient electromagnetic shielding[J]. Mater Chem Phys, 2023, 304: 127797.
[57] KHUSHNOOD R A, AHMAD S, SAVI P, et al. Improvement in electromagnetic interference shielding effectiveness of cement composites using carbonaceous nano/micro inerts[J]. Constr Build Mater, 2015, 85: 208−216.
[58] WANG X, SHU J, CAO W, et al. Eco-mimetic nanoarchitecture for green EMI shielding[J]. Chem Eng J, 2019, 369: 1068−1077.
[59] XU Y, LIN Z, YANG Y, et al. Integration of efficient

microwave absorption and shielding in a multistage composite foam with progressive conductivity modular design[J]. Mater Horiz, 2022, 9(2): 708−719.
[60] GAO S, DING J, WANG W, et al. Carbon foam/reduced graphene oxide/paraffin composite phase change material for electromagnetic interference shielding and thermal management[J]. J Energy Storage, 2023, 58: 106355.
[61] PENG Q, LI Y, GAO C, et al. MXene/bacterial cellulose/Fe_3O_4/methyltrimethoxylsilane flexible film with hydrophobic for effective electromagnetic shielding[J]. Int J Biol Macromol, 2023, 243: 125195.
[62] CHEN C, FENG W, WU W, et al. A highly strong PEDOT modified wood towards efficient electromagnetic interference shielding[J]. Ind Crops Prod, 2023, 202: 117109.
[63] XU Z, DOU T, WANG Y, et al. Three-dimensional-printed carbon nanotube/polylactic acid composite for efficient electromagnetic interference shielding[J]. Polymers-basel, 2023, 15(14): 3080.
[64] LUO Y, GUO Y, WEI C, et al. Lightweight, compressible, and stretchable composite foams for ultra-efficient and high-stable electromagnetic interference shielding materials[J]. Carbon, 2023, 215: 118480.
[65] GHAFFARKHAH A, HASHEMI S A, ROSTAMI S, et al. Ultra-flyweight cryogels of MXene/graphene oxide for electromagnetic interference shielding[J]. Adv Funct Mater, 2023, 33(50): 2304748.

Fe_3O_4/中间相煤沥青基活性复合炭泡沫制备及其电磁屏蔽和吸波性能调控

葛媛媛[1]，王禹哲[1]，徐国忠[1,*]，朱亚明[1]，袁　霞[2,*]，史桂梅[3]，钟祥云[1]

（1. 辽宁省煤化工工程研究中心, 辽宁省煤化工专业技术创新中心, 辽宁科技大学 化学工程学院, 鞍山 114051, 中国；
2. 沈阳理工大学 材料科学与工程学院, 沈阳 110159, 中国; 3. 沈阳工业大学 理学院, 沈阳 111003, 中国）

摘　要：目前，开发兼具微波吸收（MWA）和电磁干扰（EMI）屏蔽性能的材料受到了广泛关注。本研究以中间相煤沥青原料，采用高压热解法制得具有三维互连胞状孔结构的中间相沥青基炭泡沫（MPCF）。结果表明，MPCF 的三维互连胞状孔有效地促进了电磁波的多次反射。在厚度为 2.7 mm 时，MPCF 的最小反射损耗（RL_{min}）和有效吸收带宽（EAB）分别达到 −37.84 dB 和 5.44 GHz。在 X 波段下，MPCF 的平均总电磁屏蔽效能（SE_T）为 26.52 dB。利用 KOH 活化 MPCF 制得中间相沥青基活性炭泡沫（A-MPCF）。结果表明，在 X 波段下，A-MPCF 的平均 SE_T 达到 103 dB。这归因于经过 KOH 活化后，A-MPCF 的胞状孔孔壁表面嵌布着丰富的纳米孔，致使电磁波在孔胞壁表面的多次反射由多次近镜面转变为漫反射。A-MPCF 的反射系数（R）从 0.78 增加到 0.90。为了降低 A-MPCF 的 R 值，进一步采用水热合成法在 A-MPCF 的孔胞壁表面原位生长 Fe_3O_4 纳米粒子制得 Fe_3O_4/中间相沥青基活性炭泡沫（Fe_3O_4/A-MPCF）。结果表明，引入 Fe_3O_4 纳米粒子后，Fe_3O_4/A-MPCF 的 MWA 性能略有下降，但其 R 值从 0.90 显著降低至 0.74。该研究为综合调控吸波性能和电磁屏蔽性能提供一条研究思路。

关键词：炭泡沫；微波吸收；电磁干扰屏蔽；中间相沥青
中图分类号：TQ535　　**文献标识码：**A

作者简介：



葛媛媛（1996），博士研究生，从事煤基炭材料的制备及其储能和电磁干扰屏蔽应用研究，E-mail：yuanyuan_ge1996@163.com。



袁霞（1975），高级实验师，长期从事无机非金属材料和功能材料研究，E-mail：yuanxia126@126.com。



徐国忠（1973），教授，博士生导师，长期从事煤焦化和煤基新材料制备与应用基础研究，E-mail：gz_xu@163.com。